





Article

# Joint analysis of the iron emission in the optical and near-infrared spectrum of I Zw 1

Denimara Dias dos Santos <sup>1,2,†\*</sup> , Swayamtrupta Panda <sup>3,†\*</sup> , Alberto Rodríguez-Ardila <sup>1,3</sup> , Murilo Marinello <sup>3</sup> 

<sup>1</sup> Divisão de Astrofísica, Instituto Nacional de Pesquisas Espaciais (INPE), Avenida dos Astronautas 1758, São José dos Campos, 12227-010, SP, Brazil.

<sup>2</sup> Istituto Nazionale di Astrofisica (INAF), Osservatorio Astronomico di Padova, 35122 Padova, Italy

<sup>3</sup> Laboratório Nacional de Astrofísica (LNA), Rua dos Estados Unidos 154, Bairro das Nações. CEP 37504-364, Itajubá, MG, Brazil

\* Correspondence: denimara.santos@inpe.br; spanda@lna.br

† These authors contributed equally to this work.

**Abstract:** Constraining the physical conditions of the ionized media in the vicinity of an active supermassive black hole (SMBH) is crucial to understanding how these complex systems operate. Metal emission lines such as iron (Fe) are useful probes to trace the gaseous media's abundance, activity, and evolution in these accreting systems. Among these, the FeII emission has been the focus of many prior studies to investigate the energetics, kinematics, and composition of the broad-emission line region (BELR) from where these emission lines are produced. In this work, we present the first simultaneous FeII modeling in the optical and near-infrared (NIR) regions. We use CLOUDY photoionization code to simulate both spectral regions in the wavelength interval 4000 - 12000 Å. We compare our model predictions with the observed line flux ratios for I Zw 1 - a prototypical strong FeII-emitting active galactic nuclei (AGN). This allows putting constraints on the BLR cloud density and metal content that is optimal for the production of the FeII emission, which can be extended to I Zw 1-like sources, by examining a broad parameter space. We demonstrate the salient and distinct features of the FeII pseudo-continuum in the optical and NIR, giving special attention to the effect of micro-turbulence on the intensity of the FeII emission.

**Keywords:** galaxies: active; (galaxies:) quasars: emission lines; (galaxies:) quasars: supermassive black holes; accretion, accretion disks; radiation mechanisms: thermal; radiative transfer; methods: numerical; methods: observational; techniques: spectroscopic



**Citation:** D. Dias dos Santos; S. Panda; A. Rodríguez-Ardila; M. Marinello.

Joint analysis of the iron emission in the optical and near-infrared spectrum of I Zw 1. *Physics* **2023**, *1*, 1–17. <https://doi.org/>

Received:

Revised:

Accepted:

Published:



**Copyright:** © 2023 by the authors. Licensee MDPI, Basel, Switzerland. This article is an open access article distributed under the terms and conditions of the Creative Commons Attribution (CC BY) license (<https://creativecommons.org/licenses/by/4.0/>).

## 1. Introduction

Active Galactic Nuclei (AGNs) are harbored within the central cores of galaxies and host active supermassive black holes (SMBHs) at their very centers. The radiation originates from the heating of material that is drawn toward the SMBH and subsequently triggers ionization within the gas and metal-rich environment surrounding these systems [1,2]. The appearance of AGNs can vary based on the observer's perspective due to their intricate geometry [3,4]. This phenomenon also becomes evident in their observed spectra.

AGNs are further classified in terms of the types of emission line profiles they demonstrate in their observed spectrum. Sources displaying a combination of broad (permitted and semi-permitted) as well as narrow forbidden emission line profiles are categorized as Type I sources, while those lacking broad emission lines are classified as Type-II [1,5–7]. This study exclusively concentrates on Type-I sources and their emissions. The origin of the broad emission lines can be traced back to a region located around 0.01 - 0.1 parsecs away from the central ionizing source. This measurement is derived through the widely recognized technique of reverberation mapping, which has been applied to a substantial sample of over 200 AGNs to date [8–14]. This region, known as the broad line region

arXiv:2401.02936v1 [astro-ph.GA] 5 Jan 2024

(BLR), contributes significantly to the emissions observed in a typical Type-I AGN spectrum [10,11,15–36]. Notably, among the salient BLR emission features is the FeII emission, encompassing a wavelength range from ultraviolet (UV) to near-infrared (NIR) [37–39].

The emission from FeII is remarkable in the Type-I AGN spectra, primarily due to the aggregation of an extensive array of transitions, above 344,000 in number. The accumulation of the lines mimics a continuum and is hence known as a pseudo-continuum in an AGN spectrum [38,40–42]. The large number of emissions stemming from the FeII ion play a pivotal role in characterizing the energy distribution within the BLR - approximately 25% of the total emission originating in the BLR is attributed to the FeII lines [37]. Succeeding investigations have confirmed the utility of FeII emission as a surrogate for quantifying metal abundances in the BLR of AGNs across a broad range of redshifts, contributing to insights into the evolutionary trends of metallic elements within these galaxies [4,43–46].

Another crucial outcome from studies centered on FeII pertains to the development of emission templates specific to FeII. From a purely observational standpoint, the pioneering work of Boroson and Green [47] marked the inception of extracting FeII emission from a quintessential AGN FeII emitter, I Zw 1, which itself has a long and rich history [40,48–54]. The FeII template was meticulously constructed by isolating and excluding all emission lines except in the FeII. This template-driven approach continues to be employed across various studies, serving as the foundation for quantifying the optical intensity of FeII. Boroson and Green [47] played a pioneering role in comprehending FeII emission. In the same article, the authors established a robust association between the strength of FeII and various attributes of both the Broad Line Region (BLR) and the Narrow Line Region (NLR). Employing Principal Component Analysis (PCA) - a dimensionality reduction technique, they identified multiple correlations between observed spectroscopic parameters. Eigenvector1 (EV1) was the paramount correlation space among them. The EV1 from their study shows a strong correlation between the optical FeII emission within the spectral range of 4434 - 4684Å, (centered at 4570 Å), the peak intensity of [OIII]λ5007 and the Full Width at Half Maximum (FWHM) of broad component of the Hβ emission profile. This led to the well-established FWHM(Hβ) vs.  $R_{\text{FeII}}$  connection<sup>1</sup>, that is the well-known optical plane of the quasar main sequence [4,24,26,55–58]. Within this framework, FeII emission not only plays a crucial role in discerning the underlying factors driving EV1 [4] but also serves as a link between line strength and the emitting gas physics for a diverse population of Type-1 AGNs along the EV1 plane.

Regarding FeII templates, Vestergaard and Wilkes [59] progressed in the UV domain by extending the template methodology into the ultraviolet spectrum using a high-quality HST/FOS spectrum for I Zw 1. Subsequent efforts have since created several templates, effectively characterizing UV-optical FeII emission across large samples of AGNs [60–64]. Kovačević *et al.* [64] devised an innovative optical FeII template through a semi-empirical approach, combining the observed FeII emission with theoretical predictions based on allowed transitions between energy levels for the ion. By meticulously measuring individual FeII multiplet groups, they achieved a better overall agreement and were successful in getting an improved estimate for the  $R_{\text{FeII}}$ . Reproducing FeII emission in sources similar to I Zw 1 has been challenging, as empirical templates struggle to replicate specific features in observed spectra. In a recent development, Park *et al.* [65] introduced a new template based on the Mrk 493 spectrum to improve the modeling of FeII emission in I Zw 1-like sources.

Significant strides in predicting near-infrared (NIR) FeII spectra were accomplished by Sigut and Pradhan [66] and Sigut and Pradhan [41] through their utilization of the Lyα fluorescence excitation mechanism to elucidate FeII emission within the wavelength range of, 8500 - 9500 Å. This Lyα process exclusively governs the stimulation of energy levels reaching up to 13.6 eV, giving rise to the emission lines observed within this spectral segment. This assertion was corroborated by observations conducted by Rodriguez-Ardila *et al.* [67]. A semi-empirical template for NIR FeII emissions was later developed by Garcia-

<sup>1</sup>  $R_{\text{FeII}}$  is usually the ratio of the integrated FeII emission within 4434 - 4684Å to the broad Hβ emission.

Rissmann *et al.* [68], combining an observed spectrum of I Zw 1 with theoretical models from prior works by Sigut and Pradhan [41], Sigut *et al.* [42], Sigut and Pradhan [66]. More recently, this semi-empirical template was successfully applied in the NIR Fe II modeling in several AGNs spectra by Marinello *et al.* [39,69].

It is important to note here that the NIR spectrum exhibits FeII emission lines that are either isolated or semi-isolated, in contrast to the UV-optical region (see Figure 1). This feature provides a distinct advantage by enabling a more precise and reliable determination of the FeII emission line properties. The FeII lines around the 1-micron region at  $\lambda 9997$ ,  $\lambda 10502$ ,  $\lambda 10863$  and  $\lambda 11127$  are the most intense among the FeII lines [67,70,71].

Recent research [69] has highlighted the intrinsic correlation between FeII emission in the optical and near-infrared spectral regions. Due to the intricacies of FeII ion's behavior and the challenges associated with modeling its emission, researchers have been prompted to explore alternative approaches for investigating the FeII emitting gas [72,73]. Observational and photoionization modeling works have been indicating that less complex ions, such as CaII triplet ( $\lambda\lambda 8498\text{\AA}$ ,  $8542\text{\AA}$ , and  $8662\text{\AA}$ , also known as CaT), and OI lines at  $\lambda 8446$  and  $\lambda 11287$ , can serve as proxies for studying the spatial distribution of FeII emitting gas [67,69,72–74].

The FeII emission is dependent on the BLR temperature and gas density, and also on other parameters such as composition and Brownian motion within the BLR cloud – high temperature ( $\sim 5000 - 10000$  K), relatively high density ( $\log n_{\text{H}} = 10 - 12 \text{ cm}^{-3}$ ), super-solar abundances and micro-turbulence of the order of  $\sim 100 \text{ km s}^{-1}$  have been shown to positively impact the production of the FeII emission, especially in the UV and optical [4,44,75,76]. In a recent study [77], we assessed the NIR FeII emission in I Zw 1 under low column density regime ( $10^{22} \text{ cm}^{-2}$ ). In this current work, we make a comprehensive analysis of the influence of micro-turbulence on NIR emission, over a broad range of cloud densities and metal content, in conjunction with the optical region.

We aim to model the FeII emission to understand the line formation and the nature of the physical conditions in AGN with strong FeII emission, exploring how changing metal content and micro-turbulence effectively increases the FeII optical and NIR emissions simultaneously. For this purpose, we investigate three cases of micro-turbulence velocities within the ionized media, i.e., 0, 10, and  $100 \text{ km s}^{-1}$  and their impact on the optical and NIR FeII emission (based on the previous study by Panda [74] which focused only on recovering the optical FeII emission). The inclusion of the micro-turbulence parameter has been shown to augment the FeII emission line intensity in the optical and UV regions, due to the increase in the overall random, Brownian motion of the ions within the cloud [46,76,78]. This is the first study that tests the effect of micro-turbulence and metal content on the production of NIR FeII emission, along with the optical FeII emission.

The paper is organized as follows: Section 2 presents the observational spectroscopic data in the optical and NIR for I Zw 1. Section 3 describes the extraction of the FeII emission in the optical and NIR regime and estimation of the corresponding FeII strengths from the observed spectra. In Section 4, we demonstrate the modeling setup using the photoionization code CLOUDY [79]. Results are highlighted in Section 5, followed by a brief discussion in Section 6. We summarize our findings from this study in Section 7.

## 2. I Zw 1 the prototypical FeII emitter

The I Zwicky 1 (I Zw 1) is a nearby ( $z=0.061$ ) Narrow-line Seyfert 1 galaxy (NLS1), considered a prototypical FeII emitter, and widely studied in the literature [37,59,70,80,81]. NLS1s, a subclass of classical Type-I AGNs, display a narrower-to-broader range of  $H\beta$  line widths compared to classical Seyfert-I galaxies, which typically feature  $\text{FWHM}(H\beta) < 2000 \text{ km s}^{-1}$  and a flux ratio,  $[\text{OIII}]\lambda 5007/H\beta < 3$  [82].

The I Zw 1 spectrum has a rich historical record of UV, optical, and NIR studies [47,59,64,68]. Recent reverberation mapping estimated the BLR's distance of the line-emitting BLR from the central ionizing source,  $R_{\text{BLR}}=37.2$  light-days [81], a crucial parameter in our model that allows to minimize the degeneracies in our models.

To perform the optical and NIR analysis, we use the reduced and available spectra of the I Zw 1 from previous works [67–69,71]. The NIR spectrum was observed using the 3.2 m IRTF telescope (NASA Infrared Telescope Facility) at Mauna Kea, Hawaii-USA in 2000 (PI: Rodríguez-Ardila). It employed the SpeX spectrograph in cross dispersion mode (SXD) covering the wavelength interval 0.8 - 2.4 microns, and photometric bands zJHK, with a spectral resolution,  $R = 2000$  corresponding to the  $0.8'' \times 15''$  slit. Rodríguez-Ardila *et al.* [67] and Riffel *et al.* [71] presented in detail the reduced spectrum and related observational information. The optical counterpart region was obtained from the published work of Rodríguez-Ardila *et al.* [67]. The optical spectrum was obtained at the CASLEO Observatory (Complejo Astronómico el Leoncito — San Juan, Argentina), employing the REOSC spectrograph in long slit mode covering the range 3500 - 6800 Å with resolution is  $0.10 \text{ \AA pixel}^{-1}$ .

### 3. Optical and NIR FeII Templates

The FeII pseudo-continuum is comprised of a multitude of permitted FeII lines spanning from the UV to the NIR spectral regions, necessitating the use of templates for accurate modeling. In the optical domain, we used the empirical FeII template by Boroson and Green [47] derived from the spectrum of I Zw 1, the archetypal Narrow-Line Seyfert 1 (NLS1) galaxy. In the NIR range, we employed the semi-empirical template from Garcia-Rissmann *et al.* [68]. These models encompass approximately 1915 lines, within the wavelength range of 8000 - 11600 Å. The FeII spectrum was synthesized using the template, where first we widened it based on the width of the 10502 Å line, and then scaled the template to match with the observed spectrum. We use the 10502 Å line as it is the most isolated FeII line in this region, thus allowing for accurate measurement of the overall FeII intensity. The best-fit template was determined by minimizing the chi-square value at, 10502 Å. Figure 1 illustrates the spectral fitting and component decomposition for the optical and NIR region for I Zw 1. The estimation of flux uncertainty is based on the standard deviation of the best-fitted model, considering the spectrum within  $3\sigma$  of the lines of interest. For the ratios, we employed error propagation to estimate their uncertainties (see Table 1). In NLS1s, BLR emission line profiles are best represented using Lorentzian, while those of Type-I AGN with broader lines follow Gaussian shapes [83]. We fit the emission lines using the LMFIT library from Python, employing Lorentzian profiles to represent the BLR components, where the  $\chi^2$  minimizes the residual left after subtraction of the fitted profile. For lines emitted by the Narrow-line Region (NLR), we employ only Gaussian components. This procedure enabled us to measure the integrated flux, FWHM, and centroid position of the lines of interest for this study.

From these spectra and template fits, we obtain the optical FeII and NIR intensities and their respective ratios to the nearest Hydrogen line, where for the optical FeII we obtained  $R_{4570} = 1.62 \pm 0.06$ . Our findings are similar to previous works ( $\sim 1.47$  [7]). For  $R_{1\mu m}$ , we observe a discrepancy between our findings and the results reported by Marinello *et al.* [69] where they recover a ratio,  $R_{1\mu m} = 1.81 \pm 0.08$ . It is crucial to clarify that the value of 1.81 is derived from the study by Marinello *et al.* [69], and not from our current investigation. This value, from our analysis, is much smaller. We refer the readers to Table 1. The noted disparity is attributed to differing methodologies employed in the two studies. Specifically, Marinello *et al.* [69] estimated measurements corresponding to  $Pa\alpha$  and utilized the theoretical lines' ratio from Garcia-Rissmann *et al.* [68] to re-scale to  $Pa\beta$  intensity. In contrast, our approach involves the estimation of the flux of the broad component of  $Pa\gamma$ . We opted for the utilization of  $Pa\gamma$  rather than  $Pa\beta$ , as the latter is situated within a telluric spectral region [see e.g., 39].

We investigated how the ratio between  $Pa\gamma$  and  $Pa\beta$  evolves under varying gas physical conditions from our CLOUDY simulations (see Appendix A1) instead of using the theoretical value for  $Pa\beta/Pa\gamma$  (i.e., 0.8531). In Figure A1, we highlight the dependence of the ratio on the cloud density as a function of the a range of metal content that is assumed in this work using CLOUDY photoionization code. The value of the  $Pa\beta/Pa\gamma$

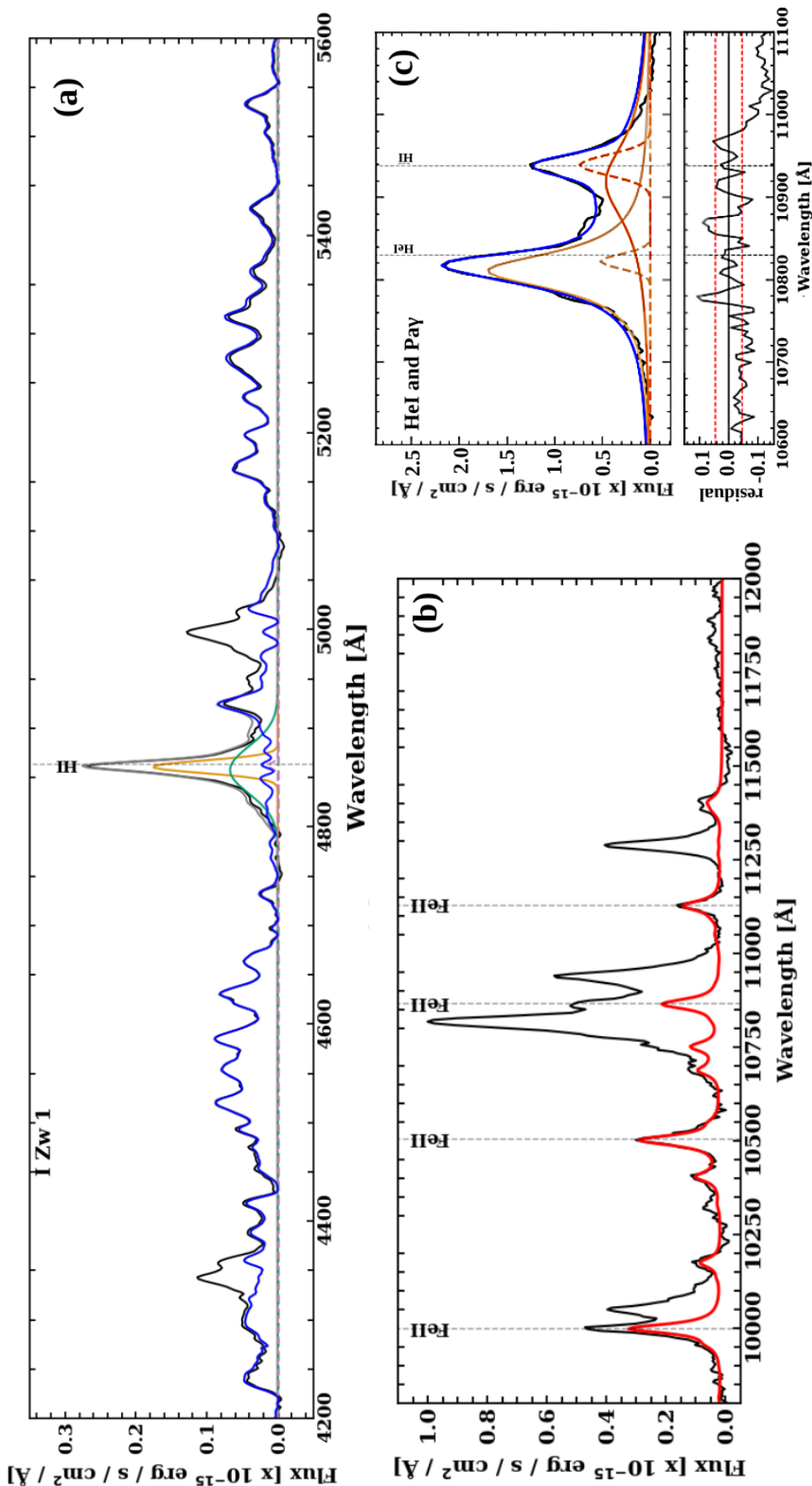


Figure 1. Three panels depicting spectra of galaxy I Zw 1. The (a) panel shows the optical spectrum (the observed spectrum is shown in black) with H $\beta$  emission line fits: green represents the outflow component, yellow is the BLR component, and orange-dashed indicates a faint narrow component. The blue curve represents the optical FeII template. The (b) displays the near-infrared spectrum in black with the fit of the semi-empirical Garcia-Rissmann et al. [68] template in red, highlighting four main NIR FeII lines used to estimate the 1-micron intensity. In addition, (c) panel shows Pa $\gamma$ -HeI line blend with HeI, where the solid line in orange represents the BLR components, while the dashed lines imply the NLR components.



**Table 1.** Values measured from the near-infrared and optical spectra of I Zw 1, where the fluxes are in units of  $10^{-14}$  erg s $^{-1}$  cm $^{-2}$  Å $^{-1}$ . The errors for 1-micron values are respectively 0.15 and 0.47, derived from the values of 1.48 and 0.46. The flux errors are also reported side-by-side with their respective measured values.

FeII $\lambda$ 10502	FeII $\lambda$ 9998	FeII $\lambda$ 10863	FeII $\lambda$ 11127	Pa $\gamma$	R $_{1\mu m}$	H $\beta$	FeII $\lambda$ 4570	R $_{4570}$
2.70 $\pm$ 1.38	4.13 $\pm$ 1.06	0.150 $\pm$ 0.17	2.32 $\pm$ 1.29	5.96 $\pm$ 0.83	0.46 $\pm$ 0.47 - 1.48 $\pm$ 0.15	10.30 $\pm$ 1.84	16.70 $\pm$ 2.80	1.62 $\pm$ 0.06

ratio varies between 1.05 - 3.38. We assume a fixed column density ( $=10^{24}$  cm $^{-2}$ ) with no micro-turbulence for this analysis. We then derive the R $_{1\mu m}$  estimates based on the calculated minimum and maximum value of the ratios obtained from these simulations which we detail in the next section. We re-scale the Pa $\gamma$  observed flux to get the flux for Pa $\beta$  (for the minimum and maximum values of their ratio) and estimate the minimum and maximum values for the intensity of FeII 1-micron lines. Consequently, we obtained a range of values for R $_{1\mu m}$  = 0.46 $\pm$ 0.47, and 1.48 $\pm$ 0.15, respectively.

#### 4. Photoionization modelling

The range of the physical conditions, used in this work, was based on previous approaches [73,74,77]. We employ the default model for the FeII ion in CLOUDY, i.e., the one defined by Verner *et al.* [38], which includes 371 levels ranging in energy up to 11.6 eV, and 68,635 transitions to keep the consistency with previous studies in low column density regime[77].

We carry out numerical simulations using CLOUDY v17.03 [79]. To constrain the number of free parameters to three, we adopt the following fixed values: the luminosity at 5100 Å,  $L_{5100} = 3.19 \times 10^{44}$  erg s $^{-1}$  from Kaspi *et al.* [84], the BLR radius determined via reverberation mapping,  $R_{BLR} = 37.2$  light-days, based on Huang *et al.* [81], and a cloud column density  $N_H = 10^{24}$  cm $^{-2}$  as concluded from earlier studies involving the recovery of the optical FeII emission in this source [73,85]. Also, we adopt the spectral energy distribution for I Zw 1 from Panda *et al.* [73] as the radiation field in our simulations. Thus, the remaining free parameters are: (i) the cloud mean hydrogen density,  $n_H$  which ranges between  $10^9 - 10^{14}$  cm $^{-3}$  and (ii) the metal content in the cloud in the range of  $0.1 \leq Z \leq 10$  (in solar units), estimated using the GASS10 module [86]. Moreover, we incorporate two scenarios for internal random motions within the BLR clouds, specifically micro-turbulence ( $V_{turb}$ ) of 10 and 100 km s $^{-1}$ . The micro-turbulence in the BLR is caused by random motions of photons within the ionized gas, which is likely triggered by magnetic fields in the confined clouds [87,88] and acts as a secondary contributor to the overall line width, as has been shown in previous studies (e.g., Kollatschny and Zetzl [89]). We assume the values for the micro-turbulent velocity based on previous works, which were successful in modeling the FeII emission in the UV region for I Zw 1 about 10-30km s $^{-1}$  [75]. In addition, Panda *et al.* [76], Panda [85] find that a micro-turbulence velocity between 10-100 km s $^{-1}$  can reproduce the FeII emission in the optical region. Additionally, as we aim to compare the effect of using micro-turbulence in the gas, we perform simulations in the absence of micro-turbulence in the gas ( $V_{turb} = 0$  km s $^{-1}$ ). This results in a total of 609 model combinations:  $V_{turb}$  (3)  $\times$   $n_H$  (29)  $\times$   $Z$  (7).

#### 5. Results

We derive from CLOUDY models the optical FeII and the NIR FeII ratio, denoted as R $_{4570}$  and R $_{1\mu m}$ , respectively. The R $_{4570}$  represents the ratio of the flux of optical FeII multiplets 37, 38, within the range 4434 - 4684 Å to the flux of H $\beta$  broad component [7,47]. The R $_{1\mu m}$  is calculated as the ratio of the combined fluxes from the four NIR prominent isolated FeII lines at wavelengths  $\lambda$ 9997,  $\lambda$ 10502,  $\lambda$ 10863, and  $\lambda$ 11127 to the flux of Pa $\beta$  broad component [67]. Rodriguez-Ardila *et al.* [67] and Marinello *et al.* [69] demonstrate that the optical and NIR intensities are correlated, indicating that both emissions should have origin and excitation mechanisms in common.

In the optical FeII emission, the micro-turbulence effect has been extensively studied [74,75], but not in the NIR. In this work, for the first time, we study the micro-turbulence effect applied to the NIR FeII region. The results are shown in Figure 2 for the column density scenario of  $10^{24} \text{ cm}^{-2}$  for optical (upper panels) and NIR (lower panels) spectral regions. The diagnostic diagrams in the same figure show the outcomes for  $V_{turb}$  values of 0, 10, and  $100 \text{ km s}^{-1}$ , for  $R_{4570}$  and  $R_{1\mu m}$  intensities as a function of the local cloud density. In each of the panels in Figure 2, we observe how the intensities vary with different metal content levels in the BLR clouds depicted using the color gradient. We further highlight the observed ratios,  $R_{4570}$  and  $R_{1\mu m}$ , and their associated uncertainties, obtained by fitting the observed spectra, using the gray and blue shaded regions, respectively.

### 5.1. No micro-turbulence

Our result without micro-turbulence (i.e., at  $0 \text{ km s}^{-1}$ ) is shown in the left panels of Figure 2, where we compare the simulated results from CLOUDY with the observed values for optical and NIR,  $R_{4570} = 1.62 \pm 0.06$  and  $R_{1\mu m} = 0.46\text{--}1.48$ , respectively, represented by the gray and blue bands<sup>2</sup>. Here, the widths of the gray bands account for the uncertainties associated with the ratios. The results show that we can reproduce  $R_{4570}$  with a metal content above  $3 Z_{\odot}$  and with a local hydrogen density between  $10^{10.75}\text{--}10^{12.50} \text{ cm}^{-3}$ . Moreover, from the NIR results, to reproduce  $R_{1\mu m}$ , it is necessary to have a local hydrogen densities range from  $10^{9.00}$  to  $10^{11.50} \text{ cm}^{-3}$ , and a metal content above  $3 Z_{\odot}$ . These results demonstrate a comparable physical parameter range to reproduce the FeII strengths for I Zw 1 in the optical and NIR regimes within our setup.

### 5.2. Applying micro-turbulence

Previous studies [73,75] demonstrated that the value obtained for  $R_{4570}$  in high metal content simulations can be achieved by increasing the micro-turbulent velocity. To investigate how changing metallicity and micro-turbulence can increase both optical and NIR emissions simultaneously, we include two cases of micro-turbulent velocity, at 10 and  $100 \text{ km s}^{-1}$ , and compare it with the default case (i.e., with no micro-turbulence). We expect that the micro-turbulence in the gas increases the Brownian motion within the cloud and allows for the FeII ions to receive preferentially more ionizing photons, consequently leading to an increase in the intensity of the FeII lines.

The results using micro-turbulence of 10 and  $100 \text{ km s}^{-1}$  are shown in Figure 2 in the middle and right panels, respectively. Our results for the optical region reveal that the FeII at  $4570 \text{ \AA}$  strength increases with the increase in micro-turbulence, as expected from previous works [73,74].

On the other hand, the results in the NIR show a different behavior compared to the ones in the optical, as presented in Figure 2. Considering a single case with  $n_{\text{H}} = 10^{12} \text{ cm}^{-3}$ , solar metallicity, and  $V_{turb} = 10 \text{ km s}^{-1}$  (see Figure 2 lower middle panel),  $R_{1\mu m}$  is approximately  $\sim 0.2$ , whereas at  $100 \text{ km s}^{-1}$ , it dropped to  $\sim 0.05$  (see Figure 2 lower right panel). In contrast, the case with no micro-turbulence produces an  $R_{1\mu m}$  value of  $\sim 0.1$  (see Figure 2 lower left panel). Notably, the absence of micro-turbulence results in lower  $R_{1\mu m}$  values compared to the scenario with  $V_{turb} = 10 \text{ km s}^{-1}$ , as expected, based on the results obtained in the optical regime. Although, for metallicities above solar,  $R_{1\mu m}$  values overall decrease when compared to scenarios without micro-turbulence. The  $R_{1\mu m}$  appears to be suppressed and fails to increase as expected from the optical results. For example, when we consider the highest metallicity value of  $10 Z_{\odot}$  (see Figure 2), and  $V_{turb} = 10 \text{ km s}^{-1}$ , and  $100 \text{ km s}^{-1}$  the maximum FeII ratio in the NIR is, respectively,  $\sim 0.8$ , and  $\sim 0.6$ , whereas in the zero micro-turbulence case, this ratio approaches  $\sim 1.2$ .

To comprehend this intriguing behavior from our CLOUDY simulations, Figure 3 provides a comparison of the FeII pseudo-continuum in the spectral region  $9500\text{--}11500 \text{ \AA}$  for a fixed local hydrogen density ( $10^{10.5} \text{ cm}^{-3}$ ) for three scenarios: without micro-turbulence,

<sup>2</sup> the symmetric errors for 1-micron values are 0.15 and 0.47, respectively, also highlighted in Table 1.

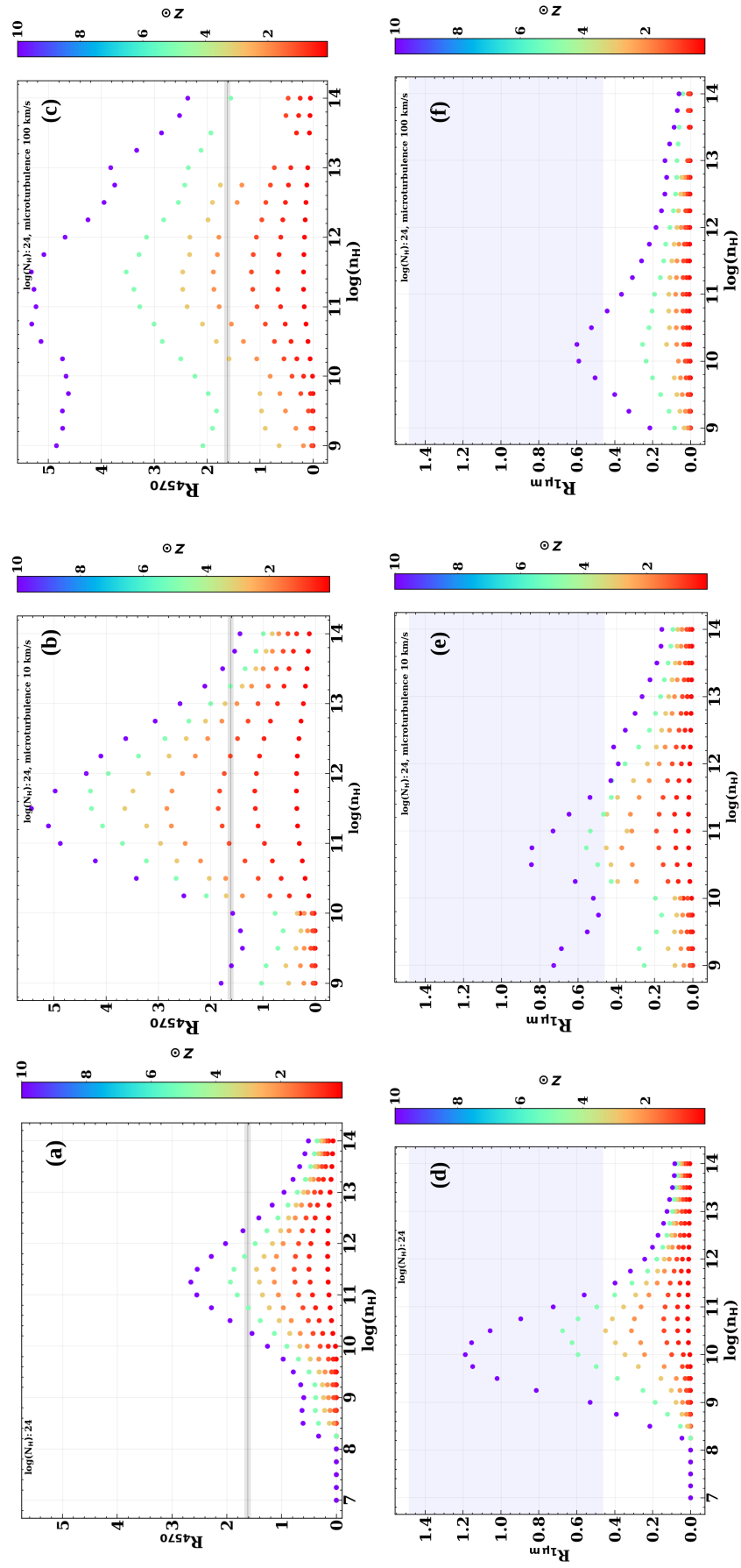


**Figure 2.** Diagnostic diagrams from simulations depicting  $R_{4570}$  intensities vs.  $n_H$  for a column density of  $10^{24} \text{ cm}^{-2}$ . The upper panels (a, b, and c) illustrate different micro-turbulent velocities, with panels (a) and (d) using  $0 \text{ km s}^{-1}$ , panels (b) and (e) corresponding to  $10 \text{ km s}^{-1}$ , and panels (c) and (f) to  $100 \text{ km s}^{-1}$ . The color bars in all cases represent metallicities ranging from  $0.1 M_{\odot}$  to  $10 M_{\odot}$ . The lower panels (d, e, and f) follow the same scheme but focus on  $R_{1,\mu m}$  ratios along the y-axis. The dark gray line represents the observed value of  $R_{4570}$ , and the light gray bar symbolizes the associated error margin. In these lower panels, the blue shaded region denotes the estimated values for  $R_{1,\mu m}$  derived from the minimum and maximum  $\text{Pa}\beta/\text{Pa}\gamma$  ratios obtained using CLOUDY simulations.



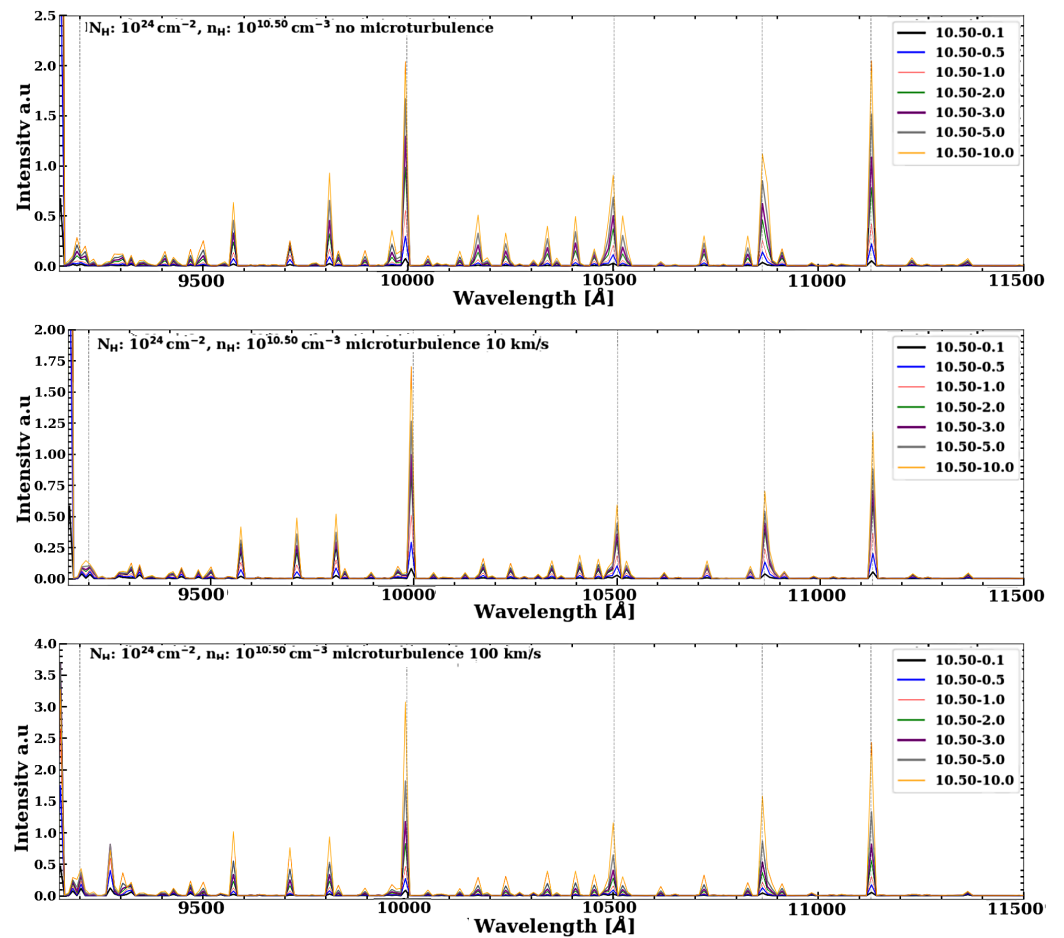


**Figure 3.** Predicted pseudo-continuum from CLOUDY simulations for FeII emission for the representative case of  $n_{\text{H}}=10^{10.5} \text{ cm}^{-3}$  using 0.1, 0.5, 1, 2, 3, 5 and  $10Z_{\odot}$  for column density case  $10^{24} \text{ cm}^{-2}$ . From top to bottom: zero micro-turbulence, 10, and  $100 \text{ km s}^{-1}$ , respectively.

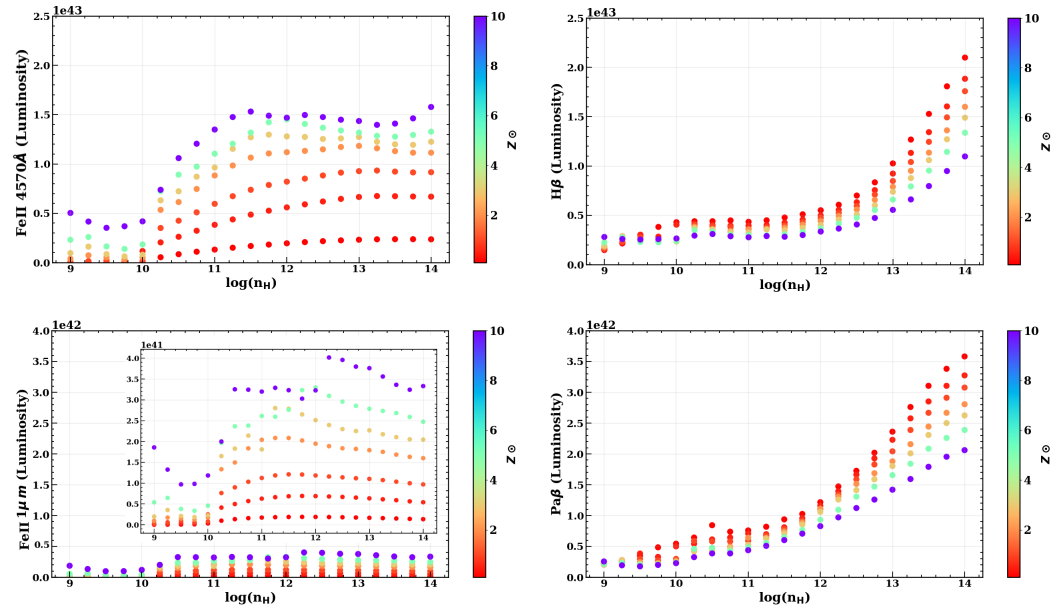


**Figure 4.** Micro-turbulence case of  $10 \text{ km s}^{-1}$ . Top panel: The y-axis represented the luminosity of the  $4570 \text{ \AA}$  bump vs. local hydrogen density, and the luminosity of  $H\beta$  line vs. local hydrogen density. The colors corresponded to the metal content cases. Down panel: The colors and the x-axis represent the same meaning. The values on the y-axis differ from NIR quantities, respectively, the sum of the luminosity of the 4 FeII 1-micron lines, and  $Pa\beta$  luminosity.

$V_{turb} = 10$  and  $100 \text{ km s}^{-1}$ . We note that the pseudo-continuum of  $V_{turb} = 10 \text{ km s}^{-1}$  exhibits less intense lines relative to the case without micro-turbulence. The case with  $100 \text{ km s}^{-1}$  shows even weaker FeII lines. Although, for the two cases with  $V_{turb} = 10$  and  $100 \text{ km s}^{-1}$ , we observe a boosting of lines, specifically between  $9600\text{--}9900 \text{ \AA}$ , which were not prominent in the spectrum in the zero micro-turbulence case.

It is important to emphasize that the intensity of the NIR FeII is characterized by the ratio of four isolated emissions to  $Pa\beta$  line, whereas the ratio in the optical is composed of blended FeII multiplets (m37, m38) normalized by the  $H\beta$  [64,90]. Hence, to understand the variations in the  $R_{1\mu m}$ , we need to study also the behavior of the  $Pa\beta$  line across the parameter space, especially under the influence of microturbulence. We notice that the luminosity of the  $Pa\beta$  emission significantly exceeds that of the NIR FeII lines. In contrast, in the optical range, both the  $H\beta$  and the optical FeII lines exhibit a similar increase in luminosity with the density, as shown in Figures 4 and 5.

Moreover, the 1-micron lines exhibit two significant excitation mechanisms, collisional and Lyman- $\alpha$  fluorescence, whereas the FeII bump at  $9200 \text{ \AA}$  is exclusively influenced by the Lyman- $\alpha$  fluorescence mechanism [67,69]. This distinction is an important indicator of the Lyman- $\alpha$  fluorescence mechanism. In our work, we note that the  $9200 \text{ \AA}$  region remains unaffected by the enhancement of micro-turbulence in the models.

## 6. Discussion

The specific influence of micro-turbulence on the NIR emission of FeII is particularly intriguing in comparison to its well-documented impact in the optical region. The optical models suggest that when micro-turbulence is introduced in the gas, it enhances the intensity of the FeII lines. Surprisingly, our simulations indicated a contrary trend in the NIR region, where the  $R_{1\mu m}$  displays lower values when microturbulence is considered than when micro-turbulence is absent.

The discrepancy between our observations and CLOUDY predictions may raise intriguing questions regarding the true impact of micro-turbulence in the near-infrared region. Initially, it was anticipated that the increased micro-turbulence would result in enhanced

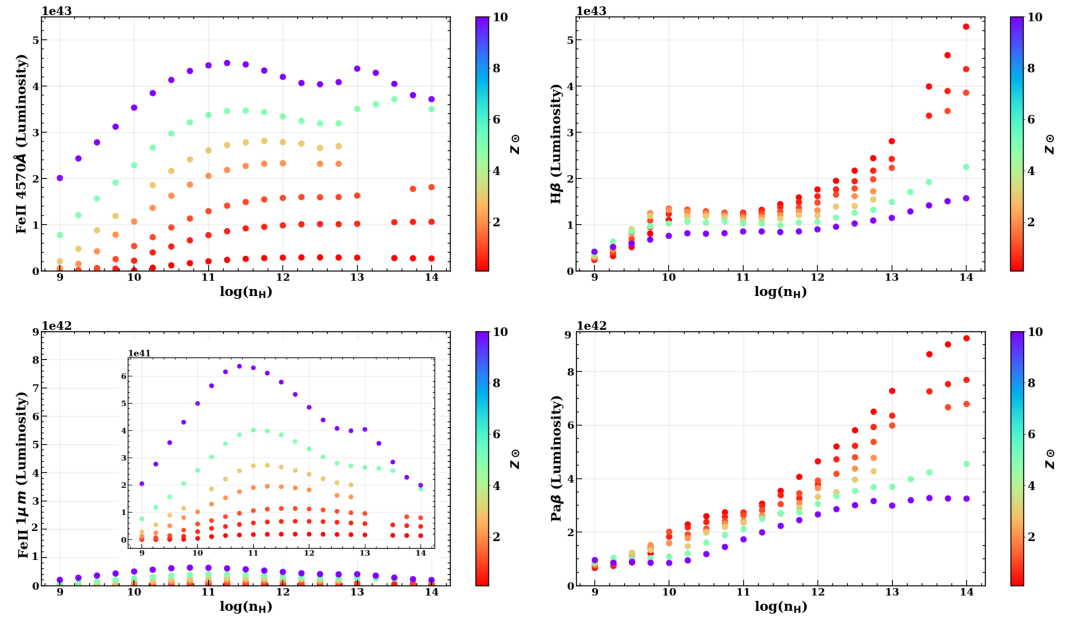


Figure 5. Same from the previous figure caption, but for micro-turbulence case of  $100 \text{ km s}^{-1}$ .

photon absorption by FeII ions, leading to an increase in the emission in this spectral region as well, as re-affirmed by the results from the FeII modeling in the optical region. This leads us to question whether micro-turbulence potentially influences the Lyman- $\alpha$  absorption by the FeII ion, thereby affecting NIR FeII emission [66–69]. A comprehensive investigation is required, which is beyond the scope of our current work.

We attribute the unexpected effects observed in the 1-micron lines to a physical limitation, where we assume a fixed value for the column density as a stopping criterion for the simulations. If we allow this parameter to be free, this can lead to a complex interplay between the column density and the metal content in the ionized gas, as found in Panda [74] in the case of the optical FeII emission. If this parameter is  $\gtrsim 10^{24.5} \text{ cm}^{-2}$ , one would have a cloud where the optical depth is  $\gtrsim 1$  where scattering effect becomes significant [see 74, for more details]. The limit at  $10^{24} \text{ cm}^{-2}$  serves to constrain the cloud's physical condition, drawing inspiration from prior works [74,75,91] wherein the radiative calculations are made under the optically thin regime. Thus, the non-monotonic behavior in the NIR may be ascribed to the collective influence of the microturbulence and cloud column density. In light of these intricate findings, further dedicated investigations are warranted to unravel the exact mechanisms at play, that includes also the advances in the available FeII atomic datasets.

Coming back to the issue of the FeII flux ratio in the NIR obtained from the observed spectrum and under the physical conditions proposed in our study, our model is not able to replicate the ratio from Marinello *et al.* [69], which is  $R_{1\mu m} \sim 1.81$ . To reproduce this value, a metal content exceeding  $10Z_{\odot}$  would be required. This would mean that the optical and NIR FeII emissions require quite different metal compositions, even though they are formed in close vicinity to each other. This latter aspect is confirmed from the correlation observed for the FWHMs for FeII in the optical and NIR [69]. Nevertheless, exploring scenarios with significantly elevated metal content may be a possibility in future research of the NIR FeII emission, especially for high-accreting sources.

Furthermore, it is worthy to emphasize the importance of investigating how the hydrogen line ratios within the BLR of an AGN vary under different physical conditions. This inquiry will significantly improve the precision of measuring the FeII ratio in the NIR for quasars with a non-reliable Pa $\beta$  line (see Marinello *et al.* [39,69] for other examples). A future study should be considered, as it has the potential to further refine our understanding of AGN environments and improve the accuracy of critical astrophysical measurements.

## 7. Conclusions

In this study, we aimed at understanding the line formation and physical conditions in a strong FeII emitter AGN, I Zw 1. We investigated how changes in micro-turbulence and metal content impact the optical and NIR emissions of FeII simultaneously. By introducing micro-turbulent velocities within the line-emitting cloud, of 10 and 100 km s<sup>-1</sup>, employing a range of cloud densities (10<sup>9</sup> - 10<sup>14</sup> cm<sup>-3</sup>), and metal content from sub-solar to 10 times solar inspired by previous works [13,73], we explored their combined effect on the recovery of the FeII intensities. Notably, this research is the first to examine the impact of micro-turbulence in the NIR regime, especially for the FeII emission, using photoionization model predictions and corroborating them with observed flux ratios obtained from archival spectra in optical and NIR for this source. While our findings align with prior findings made in the optical regime, we observed contrasting behavior in the NIR when micro-turbulence is introduced. Nonetheless, there is an overall agreement within the parameter ranges studied in the two wavelength regimes. A set of physical conditions can simultaneously reproduce optical and NIR FeII intensities, with n<sub>H</sub> = 10<sup>10.75</sup> - 10<sup>11.50</sup> cm<sup>-3</sup>, and a metal content ranging from 5 Z<sub>⊙</sub> ≲ Z ≲ 10 Z<sub>⊙</sub>.

We reproduced the R<sub>1μm</sub> value for I Zw 1 simultaneously in the optical and NIR. This result is significant not only for this source but is applicable also for I Zw 1-like AGNs. The ability to replicate R<sub>1μm</sub> values across these wavelengths is a novel accomplishment. In conclusion, a comprehensive future analysis of excitation mechanisms and FeII models holds significant promise for further insights into this complex study.

**Author Contributions:** The idea for the article and manuscript preparation was made by DDdS and SP. ARA and MM assisted with the editing and proofreading of the manuscript. All authors have read and agreed to the published version of the manuscript.

**Funding:** This research received no external funding.

**Data Availability Statement:** Data used in this work can be provided upon request to the corresponding authors.

**Acknowledgments:** The authors thank the Brazilian Agencies: Agency of Coordenação de Aperfeiçoamento de Pessoal de Nível Superior (CAPES), and Conselho Nacional de Desenvolvimento Científico e Tecnológico (CNPq).

**Conflicts of Interest:** The authors declare no conflict of interest.

## Abbreviations

The following abbreviations are used in this manuscript:

AGNs	Active galactic nuclei
BELR	Broad-emission line region
BLR	Broad-line region
EV1	Eigenvector 1
FWHM	Full width at half maximum
FOS	Faint Object Spectrograph
HST	Hubble Space Telescope
IRTF	Infrared Telescope Facility
NLR	Narrow-line region
NLS1	Narrow-line Seyfert 1
NIR	Near-infrared
PCA	Principal component analysis
SMBHs	Supermassive black holes
SXD	Short wavelength cross-dispersed mode
UV	Ultraviolet

## Appendix A

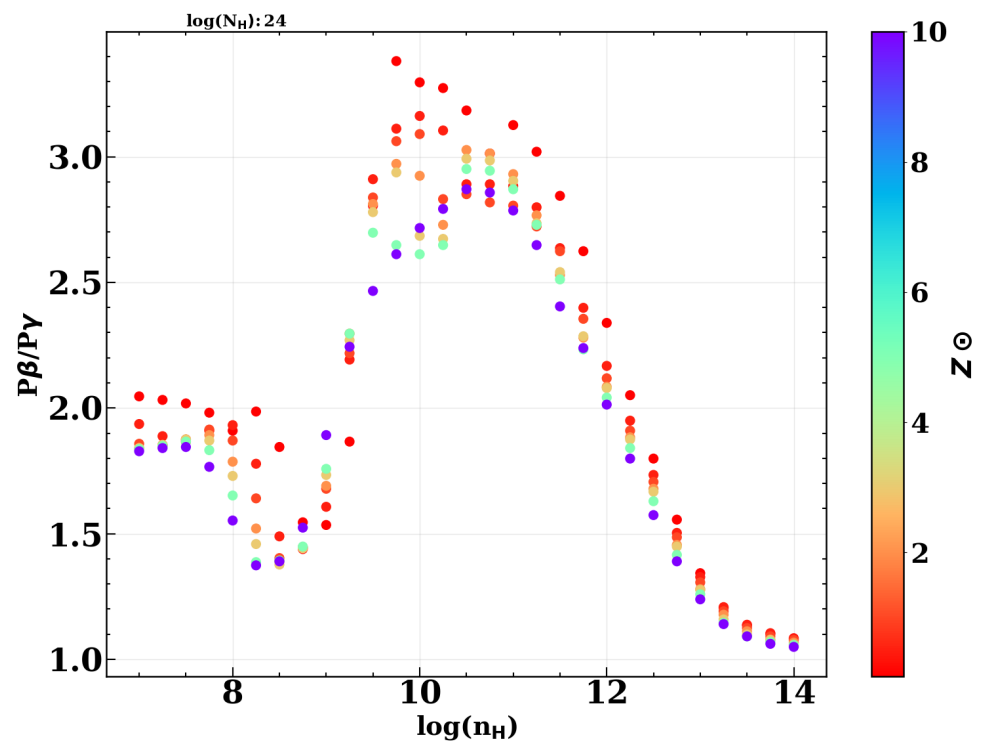


**Figure A1.** The y-axis represented the luminosity ratio for Pa $\beta$  to Pa $\gamma$  obtained from our simulations for a range of local hydrogen densities (x-axis). The colors correspond to the different metal content. The cloud column density is  $10^{24}$  cm $^{-2}$  at zero microturbulence.

## References

1. Netzer, H. Revisiting the Unified Model of Active Galactic Nuclei. *Annual Reviews in Astronomy and Astrophysics* **2015**, *53*, 365–408, [arXiv:astro-ph.GA/1505.00811]. <https://doi.org/10.1146/annurev-astro-082214-122302>.
2. Padovani, P.; Alexander, D.M.; Assef, R.J.; De Marco, B.; Giommi, P.; Hickox, R.C.; Richards, G.T.; Smolčić, V.; Hatziminaoglou, E.; Mainieri, V.; et al. Active galactic nuclei: what's in a name? *Astronomy & Astrophysics Reviews* **2017**, *25*, 2, [arXiv:astro-ph.GA/1707.07134]. <https://doi.org/10.1007/s00159-017-0102-9>.
3. Collin, S.; Kawaguchi, T.; Peterson, B.M.; Vestergaard, M. Systematic effects in measurement of black hole masses by emission-line reverberation of active galactic nuclei: Eddington ratio and inclination. *Astronomy & Astrophysics* **2006**, *456*, 75–90, [arXiv:astro-ph/astro-ph/0603460]. <https://doi.org/10.1051/0004-6361:20064878>.
4. Panda, S.; Marziani, P.; Czerny, B. The Quasar main sequence explained by the combination of Eddington ratio, metallicity, and orientation. *The Astrophysical Journal* **2019**, *882*, 79. <https://doi.org/10.3847/1538-4357/ab3292>.
5. Antonucci, R. Unified models for active galactic nuclei and quasars. *Annual Review of Astronomy and Astrophysics* **1993**, *31*, 473–521. <https://doi.org/10.1146/annurev.aa.31.090193.002353>.
6. Urry, C.M.; Padovani, P. Unified Schemes for Radio-Loud Active Galactic Nuclei. *Publications of the Astronomical Society of the Pacific* **1995**, *107*, 803, [arXiv:astro-ph/astro-ph/9506063]. <https://doi.org/10.1086/133630>.
7. Sulentic, J.; Marziani, P.; Dultzin-Hacyan, D. Phenomenology of broad emission lines in active galactic nuclei. *Annual Review of Astronomy and Astrophysics* **2000**, *38*, 521–571. <https://doi.org/https://doi.org/10.1146/annurev.astro.38.1.521>.
8. Blandford, R.; McKee, C. Reverberation mapping of the emission line regions of Seyfert galaxies and quasars. *The Astrophysical Journal* **1982**, *255*, 419–439. <https://doi.org/10.1086/159843>.
9. Peterson, B.M.; Ferrarese, L.; Gilbert, K.M.; Kaspi, S.; Malkan, M.A.; Maoz, D.; Merritt, D.; Netzer, H.; Onken, C.A.; Pogge, R.W.; et al. Central Masses and Broad-Line Region Sizes of Active Galactic Nuclei. II. A Homogeneous Analysis of a Large Reverberation-Mapping Database. *The Astrophysical Journal* **2004**, *613*, 682–699, [arXiv:astro-ph/astro-ph/0407299]. <https://doi.org/10.1086/423269>.
10. Bentz, M.C.; Denney, K.D.; Grier, C.J.; Barth, A.J.; Peterson, B.M.; Vestergaard, M.; Bennert, V.N.; Canalizo, G.; De Rosa, G.; Filippenko, A.V.; et al. The low-luminosity end of the radius–luminosity relationship for active galactic nuclei. *The Astrophysical Journal* **2013**, *767*, 149. <https://doi.org/10.1088/0004-637X/767/2/149>.



11. Du, P.; Hu, C.; Lu, K.X.; Huang, Y.K.; Cheng, C.; Qiu, J.; Li, Y.R.; Zhang, Y.W.; Fan, X.L.; Bai, J.M.; et al. Supermassive black holes with high accretion rates in active galactic nuclei. IV. H $\beta$  time lags and implications for super-Eddington accretion. *The Astrophysical Journal* **2015**, *806*, 22.
12. Grier, C.; Pancoast, A.; Barth, A.; Fausnaugh, M.; Brewer, B.; Treu, T.; Peterson, B. The structure of the broad-line region in active galactic nuclei. II. Dynamical modeling of data from the AGN10 reverberation mapping campaign. *The Astrophysical Journal* **2017**, *849*, 146.
13. Panda, S.; Martínez-Aldama, M.L.; Zajaček, M. Current and future applications of Reverberation-mapped quasars in Cosmology. *Frontiers in Astronomy and Space Sciences* **2019**, *6*, 75. <https://doi.org/https://doi.org/10.3389/fspas.2019.00075>.
14. Shen, Y.; Grier, C.J.; Horne, K.; Stone, Z.; Li, J.I.; Yang, Q.; Homayouni, Y.; Trump, J.R.; Anderson, S.F.; Brandt, W.N.; et al. The Sloan Digital Sky Survey Reverberation Mapping Project: Key Results. *arXiv e-prints* **2023**, p. arXiv:2305.01014, [[arXiv:astro-ph.GA/2305.01014](https://arxiv.org/abs/2305.01014)]. <https://doi.org/10.48550/arXiv.2305.01014>.
15. Peterson, B.M.; Ali, B.; Horne, K.; Bertram, R.; Lamé, N.J.; Pogge, R.W.; Wagner, R.M. The Structure of the Broad-Line Region in the Seyfert Galaxy Markarian 590. *The Astrophysical Journal* **1993**, *402*, 469. <https://doi.org/10.1086/172150>.
16. Peterson, B.M.; Berlind, P.; Bertram, R.; Bochkarev, N.G.; Bond, D.; Brotherton, M.S.; Busler, J.R.; Chuvaev, K.K.; Cohen, R.D.; Dietrich, M.; et al. Steps toward Determination of the Size and Structure of the Broad-Line Region in Active Galactic Nuclei. VII. Variability of the Optical Spectrum of NGC 5548 over 4 Years. *The Astrophysical Journal* **1994**, *425*, 622. <https://doi.org/10.1086/174009>.
17. Rosenblatt, E.I.; Malkan, M.A.; Sargent, W.L.W.; Readhead, A.C.S. The Broad Emission Line and Continuum Variations of Seyfert Galaxies. II. Broad-Line Region Structure and Kinematics. *The Astrophysical Journal Supplements* **1994**, *93*, 73. <https://doi.org/10.1086/192047>.
18. Korista, K.T.; Alloin, D.; Barr, P.; Clavel, J.; Cohen, R.D.; Crenshaw, D.M.; Evans, I.N.; Horne, K.; Koratkar, A.P.; Kriss, G.A.; et al. Steps toward Determination of the Size and Structure of the Broad-Line Region in Active Galactic Nuclei. VIII. an Intensive HST, IUE, and Ground-based Study of NGC 5548. *The Astrophysical Journal Supplements* **1995**, *97*, 285. <https://doi.org/10.1086/192144>.
19. Veilleux, S.; Sanders, D.B.; Kim, D.C. A Near-Infrared Search for Hidden Broad-Line Regions in Ultraluminous Infrared Galaxies. *The Astrophysical Journal* **1997**, *484*, 92–107. <https://doi.org/10.1086/304337>.
20. Berk, D.E.V.; Richards, G.T.; Bauer, A.; Strauss, M.A.; Schneider, D.P.; Heckman, T.M.; York, D.G.; Hall, P.B.; Fan, X.; Knapp, G.; et al. Composite quasar spectra from the sloan digital sky survey. *The Astronomical Journal* **2001**, *122*, 549.
21. Kollatschny, W. Accretion disk wind in the AGN broad-line region: Spectroscopically resolved line profile variations in Mrk 110. *Astronomy & Astrophysics* **2003**, *407*, 461–472, [[arXiv:astro-ph/astro-ph/0306389](https://arxiv.org/abs/astro-ph/0306389)]. <https://doi.org/10.1051/0004-6361:20030928>.
22. Glikman, E.; Helfand, D.J.; White, R.L. A near-infrared spectral template for quasars. *The Astrophysical Journal* **2006**, *640*, 579. <https://doi.org/https://doi.org/10.1086/500098>.
23. Vestergaard, M.; Peterson, B.M. Determining Central Black Hole Masses in Distant Active Galaxies and Quasars. II. Improved Optical and UV Scaling Relationships. *The Astrophysical Journal* **2006**, *641*, 689–709, [[arXiv:astro-ph/astro-ph/0601303](https://arxiv.org/abs/astro-ph/0601303)]. <https://doi.org/10.1086/500572>.
24. Marziani, P.; Sulentic, J.W.; Negrete, C.A.; Dultzin, D.; Zamfir, S.; Bachev, R. Broad-line region physical conditions along the quasar eigenvector 1 sequence. *Monthly Notices of the Royal Astronomical Society* **2010**, *409*, 1033–1048, [[arXiv:astro-ph.CO/1007.3187](https://arxiv.org/abs/astro-ph.CO/1007.3187)]. <https://doi.org/10.1111/j.1365-2966.2010.17357.x>.
25. Pozo Nuñez, F.; Ramolla, M.; Westhues, C.; Haas, M.; Chini, R.; Steenbrugge, K.; Barr Domínguez, A.; Kaderhandt, L.; Hackstein, M.; Kollatschny, W.; et al. The broad-line region and dust torus size of the Seyfert 1 galaxy PGC 50427. *Astronomy & Astrophysics* **2015**, *576*, A73, [[arXiv:astro-ph.GA/1502.06771](https://arxiv.org/abs/astro-ph.GA/1502.06771)]. <https://doi.org/10.1051/0004-6361/201525910>.
26. Marziani, P.; Dultzin, D.; Sulentic, J.W.; Del Olmo, A.; Negrete, C.A.; Martínez-Aldama, M.L.; D’Onofrio, M.; Bon, E.; Bon, N.; Stirpe, G.M. A main sequence for Quasars, 2018. <https://doi.org/10.3389/fspas.2018.00006>.
27. MacLeod, C.L.; Green, P.J.; Anderson, S.F.; Bruce, A.; Eracleous, M.; Graham, M.; Homan, D.; Lawrence, A.; LeBleu, A.; Ross, N.P.; et al. Changing-look Quasar Candidates: First Results from Follow-up Spectroscopy of Highly Optically Variable Quasars. *The Astrophysical Journal* **2019**, *874*, 8, [[arXiv:astro-ph.GA/1810.00087](https://arxiv.org/abs/astro-ph.GA/1810.00087)]. <https://doi.org/10.3847/1538-4357/ab05e2>.
28. Wolf, J.; Salvato, M.; Coffey, D.; Merloni, A.; Buchner, J.; Arcodia, R.; Baron, D.; Carrera, F.J.; Comparat, J.; Schneider, D.P.; et al. Exploring the diversity of Type 1 active galactic nuclei identified in SDSS-IV/SPIDERS. *Monthly Notices of the Royal Astronomical Society* **2020**, *492*, 3580–3601, [[arXiv:astro-ph.HE/1911.01947](https://arxiv.org/abs/astro-ph.HE/1911.01947)]. <https://doi.org/10.1093/mnras/staa018>.
29. Fonseca Alvarez, G.; Trump, J.R.; Homayouni, Y.; Grier, C.J.; Shen, Y.; Horne, K.; Li, J.I.H.; Brandt, W.N.; Ho, L.C.; Peterson, B.M.; et al. The Sloan Digital Sky Survey Reverberation Mapping Project: The H $\beta$  Radius-Luminosity Relation. *The Astrophysical Journal* **2020**, *899*, 73, [[arXiv:astro-ph.GA/1910.10719](https://arxiv.org/abs/astro-ph.GA/1910.10719)]. <https://doi.org/10.3847/1538-4357/aba001>.
30. Rakshit, S. Broad line region and black hole mass of PKS 1510-089 from spectroscopic reverberation mapping. *Astronomy & Astrophysics* **2020**, *642*, A59, [[arXiv:astro-ph.GA/2007.07672](https://arxiv.org/abs/astro-ph.GA/2007.07672)]. <https://doi.org/10.1051/0004-6361/202038324>.
31. Schindler, J.T.; Farina, E.P.; Bañados, E.; Eilers, A.C.; Hennawi, J.F.; Onoue, M.; Venemans, B.P.; Walter, F.; Wang, F.; Davies, F.B.; et al. The X-SHOOTER/ALMA Sample of Quasars in the Epoch of Reionization. I. NIR Spectral Modeling, Iron Enrichment, and Broad Emission Line Properties. *The Astrophysical Journal* **2020**, *905*, 51, [[arXiv:astro-ph.GA/2010.06902](https://arxiv.org/abs/astro-ph.GA/2010.06902)]. <https://doi.org/10.3847/1538-4357/abc2d7>.
32. Li, S.S.; Feng, H.C.; Liu, H.T.; Bai, J.M.; Li, R.; Lu, K.X.; Wang, J.G.; Huang, Y.K.; Zhang, Z.X. Velocity-resolved Reverberation Mapping of Changing-look Active Galactic Nucleus NGC 4151 during Outburst Stage: Evidence for Kinematics Evolution of

- Broad-line Region. *The Astrophysical Journal* **2022**, *936*, 75, [arXiv:astro-ph.GA/2208.02966]. <https://doi.org/10.3847/1538-4357/ac8745>.
33. Pandey, S.; Rakshit, S.; Woo, J.H.; Stalin, C.S. Spectroscopic reverberation mapping of Quasar PKS 0736 + 017: broad-line region and black-hole mass. *Monthly Notices of the Royal Astronomical Society* **2022**, *516*, 2671–2682, [arXiv:astro-ph.GA/2209.01649]. <https://doi.org/10.1093/mnras/stac2418>.
34. Lu, K.X.; Bai, J.M.; Wang, J.M.; Hu, C.; Li, Y.R.; Du, P.; Xiao, M.; Feng, H.C.; Li, S.S.; Wang, J.G.; et al. Supermassive Black Hole and Broad-line Region in NGC 5548: Results from Five-season Reverberation Mapping. *The Astrophysical Journal Supplements* **2022**, *263*, 10, [arXiv:astro-ph.GA/2209.10853]. <https://doi.org/10.3847/1538-4365/ac94d3>.
35. Bentz, M.C.; Onken, C.A.; Street, R.; Valluri, M. Reverberation Mapping of IC 4329A. *The Astrophysical Journal* **2023**, *944*, 29, [arXiv:astro-ph.GA/2212.05954]. <https://doi.org/10.3847/1538-4357/acab62>.
36. Donnan, F.R.; Hernández Santisteban, J.V.; Horne, K.; Hu, C.; Du, P.; Li, Y.R.; Xiao, M.; Ho, L.C.; Aceituno, J.; Wang, J.M.; et al. Testing super-eddington accretion on to a supermassive black hole: reverberation mapping of PG 1119+120. *Monthly Notices of the Royal Astronomical Society* **2023**, *523*, 545–567, [arXiv:astro-ph.GA/2302.09370]. <https://doi.org/10.1093/mnras/stad1409>.
37. Wills, B.J.; Netzer, H.; Wills, D. Broad emission features in QSOs and active galactic nuclei. II—New observations and theory of Fe II and III emission. *The Astrophysical Journal* **1985**, *288*, 94–116. <https://doi.org/https://doi.org/10.1086/162767>.
38. Verner, E.; Verner, D.; Korista, K.; Ferguson, J.W.; Hamann, F.; Ferland, G.J. Numerical simulations of Fe II emission spectra. *The Astrophysical Journal Supplement Series* **1999**, *120*, 101. <https://doi.org/10.1086/313171>.
39. Marinello, M.; Rodríguez-Ardila, A.; Marziani, P.; Sigut, A.; Pradhan, A. Panchromatic properties of the extreme Fe II emitter PHL 1092. *Monthly Notices of the Royal Astronomical Society* **2020**, *494*, 4187–4202.
40. Phillips, M.M. Observations of Fe II emission in Seyfert galaxies and QSOs. *The Astrophysical Journal* **1977**, *215*, 746–754. <https://doi.org/10.1086/155408>.
41. Sigut, T.; Pradhan, A.K. Predicted Fe II emission-line strengths from active galactic nuclei. *The Astrophysical Journal Supplement Series* **2003**, *145*, 15. <https://doi.org/10.1086/345498>.
42. Sigut, T.; Pradhan, A.K.; Nahar, S.N. Theoretical Fe I–III emission-line strengths from active galactic nuclei with broad-line regions. *The Astrophysical Journal* **2004**, *611*, 81. <https://doi.org/https://doi.org/10.1086/422027>.
43. Hamann, F.; Ferland, G. The age and chemical evolution of high-redshift QSOs. *The Astrophysical Journal* **1992**, *391*, L53–L57. <https://doi.org/10.1086/186397>.
44. Baldwin, J.; Ferland, G.J.; Korista, K.; Hamann, F.; LaCluyzé, A. The origin of Fe II emission in active galactic nuclei. *The Astrophysical Journal* **2004**, *615*, 610. <https://doi.org/10.1086/424683>.
45. Martínez-Aldama, M.L.; Panda, S.; Czerny, B.; Marinello, M.; Marziani, P.; Dultzin, D. The CaFe Project: Optical Fe II and Near-infrared Ca II Triplet Emission in Active Galaxies. II. The Driver (s) of the Ca II and Fe II and Its Potential Use as a Chemical Clock. *The Astrophysical Journal* **2021**, *918*, 29. <https://doi.org/https://doi.org/10.3847/1538-4357/ac03b6>.
46. Sarkar, A.; Ferland, G.; Chatzikos, M.; Guzmán, F.; van Hoof, P.; Smyth, R.; Ramsbottom, C.; Keenan, F.; Ballance, C. Improved Fe II Emission-line Models for AGNs Using New Atomic Data Sets. *The Astrophysical Journal* **2021**, *907*, 12. <https://doi.org/https://doi.org/10.3847/1538-4357/abcaa6>.
47. Boroson, T.A.; Green, R.F. The emission-line properties of low-redshift quasi-stellar objects. *The Astrophysical Journal Supplement Series* **1992**, *80*, 109–135.
48. Phillips, M.M. The optical spectrum of I Zwicky 1. *The Astrophysical Journal* **1976**, *208*, 37. <https://doi.org/10.1086/154578>.
49. Oke, J.B.; Lauer, T.R. An analysis of the spectra of the Seyfert galaxies Markarian 79 and I Zw 1. *The Astrophysical Journal* **1979**, *230*, 360–372. <https://doi.org/10.1086/157092>.
50. Joly, M. The Fe II spectrum of Seyfert 1 galaxies and quasars. *Astronomy & Astrophysics* **1981**, *102*, 321–330.
51. Halpern, J.P.; Oke, J.B. Narrow-Line Seyfert Galaxies with Permitted Fe II Emission: Markarian 507, 5C 3.100, and I Zwicky 1. *The Astrophysical Journal* **1987**, *312*, 91. <https://doi.org/10.1086/164851>.
52. Laor, A.; Jannuzi, B.T.; Green, R.F.; Boroson, T.A. The Ultraviolet Properties of the Narrow-Line Quasar I Zw 1. *The Astrophysical Journal* **1997**, *489*, 656–671, [arXiv:astro-ph/astro-ph/9706264]. <https://doi.org/10.1086/304816>.
53. Negrete, C.A.; Dultzin, D.; Marziani, P.; Sulentic, J.W. Broad-line Region Physical Conditions in Extreme Population A Quasars: A Method to Estimate Central Black Hole Mass at High Redshift. *The Astrophysical Journal* **2012**, *757*, 62, [arXiv:astro-ph.CO/1107.3188]. <https://doi.org/10.1088/0004-637X/757/1/62>.
54. Park, D.; Barth, A.J.; Ho, L.C.; Laor, A. A New Iron Emission Template for Active Galactic Nuclei. I. Optical Template for the H $\beta$  Region. *The Astrophysical Journal Supplements* **2022**, *258*, 38, [arXiv:astro-ph.GA/2111.15118]. <https://doi.org/10.3847/1538-4365/ac3f3e>.
55. Sulentic, J.W.; Zwitter, T.; Marziani, P.; Dultzin-Hacyan, D. Eigenvector 1: An Optimal Correlation Space for Active Galactic Nuclei. *The Astrophysical Journal Letters* **2000**, *536*, L5–L9, [arXiv:astro-ph/astro-ph/0005177]. <https://doi.org/10.1086/312717>.
56. Shen, Y.; Ho, L.C. The diversity of quasars unified by accretion and orientation. *Nature* **2014**, *513*, 210–213. <https://doi.org/https://doi.org/10.1038/nature13712>.
57. Deconto-Machado, A.; del Olmo Orozco, A.; Marziani, P.; Perea, J.; Stirpe, G.M. High-redshift quasars along the main sequence. *Astronomy & Astrophysics* **2023**, *669*, A83, [arXiv:astro-ph.GA/2211.03853]. <https://doi.org/10.1051/0004-6361/202243801>.

58. Mengistue, S.T.; Del Olmo, A.; Marziani, P.; Pović, M.; Martínez-Carballo, M.A.; Perea, J.; Márquez, I. Optical and near-UV spectroscopic properties of low-redshift jetted quasars in the main sequence context. *Monthly Notices of the Royal Astronomical Society* **2023**, *525*, 4474–4496, [arXiv:astro-ph.GA/2308.06080]. <https://doi.org/10.1093/mnras/stad2467>.
59. Vestergaard, M.; Wilkes, B.J. An empirical ultraviolet template for iron emission in quasars as derived from I Zwicky 1. *The Astrophysical Journal Supplement Series* **2001**, *134*, 1. <https://doi.org/10.1086/320357>.
60. Tsuzuki, Y.; Kawara, K.; Yoshii, Y.; Oyabu, S.; Tanabé, T.; Matsuo, Y. Fe II emission in 14 low-redshift quasars. I. Observations. *The Astrophysical Journal* **2006**, *650*, 57. <https://doi.org/10.1086/506376>.
61. Kovačević-Dojčinović, J.; Popović, L.Č. The connections between the UV and optical Fe II emission lines in type 1 AGNs. *The Astrophysical Journal Supplement Series* **2015**, *221*, 35. <https://doi.org/10.1088/0067-0049/221/2/35>.
62. Dong, X.B.; Ho, L.C.; Wang, J.G.; Wang, T.G.; Wang, H.; Fan, X.; Zhou, H. The Prevalence of Narrow Optical Fe II Emission Lines in Type 1 Active Galactic Nuclei. *The Astrophysical Journal Letters* **2010**, *721*, L143. <https://doi.org/10.1088/2041-8205/721/2/L143>.
63. Dong, X.B.; Wang, J.G.; Ho, L.C.; Wang, T.G.; Fan, X.; Wang, H.; Zhou, H.; Yuan, W. What controls the Fe II strength in active galactic nuclei? *The Astrophysical Journal* **2011**, *736*, 86. <https://doi.org/10.1088/0004-637X/736/2/86>.
64. Kovačević, J.; Popović, L.Č.; Dimitrijević, M.S. Analysis of optical Fe II emission in a sample of active galactic nucleus spectra. *The Astrophysical Journal Supplement Series* **2010**, *189*, 15. <https://doi.org/10.1088/0067-0049/189/1/15>.
65. Park, D.; Barth, A.J.; Ho, L.C.; Laor, A. A New Iron Emission Template for Active Galactic Nuclei. I. Optical Template for the H $\beta$  Region. *The Astrophysical Journal Supplement Series* **2022**, *258*, 38. <https://doi.org/10.3847/1538-4365/ac3f3e>.
66. Sigut, T.; Pradhan, A.K. Ly $\alpha$  Fluorescent Excitation of Fe II in Active Galactic Nuclei. *The Astrophysical Journal* **1998**, *499*, L139. <https://doi.org/10.1086/311369>.
67. Rodríguez-Ardila, A.; Viegas, S.; Pastoriza, M.G.; Prato, L. Infrared Fe II Emission in Narrow-Line Seyfert 1 Galaxies. *The Astrophysical Journal* **2002**, *565*, 140. <https://doi.org/10.1086/324598>.
68. García-Rissmann, A.; Rodríguez-Ardila, A.; Sigut, T.; Pradhan, A. A near-infrared template derived from I Zw 1 for the Fe II emission in active galaxies. *The Astrophysical Journal* **2012**, *751*, 7. <https://doi.org/10.1088/0004-637X/751/1/7>.
69. Marinello, M.; Rodríguez-Ardila, A.; García-Rissmann, A.; Sigut, T.; Pradhan, A. The Fe II Emission in Active Galactic Nuclei: Excitation Mechanisms and Location of the Emitting Region. *The Astrophysical Journal* **2016**, *820*, 116. <https://doi.org/10.3847/0004-637X/820/2/116>.
70. Rudy, R.J.; Mazuk, S.; Puetter, R.; Hamann, F. The 1 micron Fe II lines of the seyfert galaxy I Zw 1. *The Astrophysical Journal* **2000**, *539*, 166. <https://doi.org/10.1086/309222>.
71. Riffel, R.; Rodríguez-Ardila, A.; Pastoriza, M.G. A 0.8–2.4  $\mu\text{m}$  spectral atlas of active galactic nuclei. *Astronomy & Astrophysics* **2006**, *457*, 61–70. <https://doi.org/10.1051/0004-6361:20065291>.
72. Martínez-Aldama, M.L.; Dultzin, D.; Marziani, P.; Sulentic, J.W.; Bressan, A.; Chen, Y.; Stirpe, G.M. O i AND Ca ii OBSERVATIONS IN INTERMEDIATE REDSHIFT QUASARS. *The Astrophysical Journal Supplement Series* **2015**, *217*, 3. <https://doi.org/10.1088/0067-0049/217/1/3>.
73. Panda, S.; Martínez-Aldama, M.L.; Marinello, M.; Czerny, B.; Marziani, P.; Dultzin, D. The CaFe Project: Optical Fe ii and Near-infrared Ca ii Triplet Emission in Active Galaxies. I. Photoionization Modeling. *The Astrophysical Journal* **2020**, *902*, 76. <https://doi.org/10.3847/1538-4357/abb5b8>.
74. Panda, S. The CaFe project: Optical Fe II and near-infrared Ca II triplet emission in active galaxies: simulated EWs and the co-dependence of cloud size and metal content. *Ats* **2021**, *650*, A154, [arXiv:astro-ph.GA/2004.13113]. <https://doi.org/10.1051/0004-6361/202140393>.
75. Bruhweiler, F.; Verner, E. Modeling fe II emission and revised Fe II (UV) empirical templates for the seyfert 1 galaxy I Zw 1. *The Astrophysical Journal* **2008**, *675*, 83. <https://doi.org/10.1086/525557>.
76. Panda, S.; Czerny, B.; Adhikari, T.P.; Hryniewicz, K.; Wildy, C.; Kuraszek, J.; Śniegowska, M. Modeling of the Quasar Main Sequence in the Optical Plane. *The Astrophysical Journal* **2018**, *866*, 115. <https://doi.org/10.3847/1538-4357/aae209>.
77. dos Santos, D.D.; Panda, S.; Rodríguez-Ardila, A.; Marinello, M. Modelling the strong Fe ii emission. *Boletim da Sociedade Astronômica Brasileira*, *34*, 295–299.
78. Panda, S.; Czerny, B.; Done, C.; Kubota, A. CLOUDY View of the Warm Corona. *The Astrophysical Journal* **2019**, *875*, 133, [arXiv:astro-ph.HE/1901.02962]. <https://doi.org/10.3847/1538-4357/ab11cb>.
79. Ferland, G.J.; Chatzikos, M.; Guzmán, F.; Lykins, M.L.; van Hoof, P.A.M.; Williams, R.J.R.; Abel, N.P.; Badnell, N.R.; Keenan, F.P.; Porter, R.L.; et al. The 2017 Release Cloudy. *Revista Mexicana de Astronomía y Astrofísica* **2017**, *53*, 385–438, [arXiv:astro-ph.GA/1705.10877]. <https://doi.org/10.48550/arXiv.1705.10877>.
80. Véron-Cetty, M.P.; Joly, M.; Véron, P. The unusual emission line spectrum of I Zw 1. *Astronomy & Astrophysics* **2004**, *417*, 515–525. <https://doi.org/10.1051/0004-6361:20035714>.
81. Huang, Y.K.; Hu, C.; Zhao, Y.L.; Zhang, Z.X.; Lu, K.X.; Wang, K.; Zhang, Y.; Du, P.; Li, Y.R.; Bai, J.M.; et al. Reverberation mapping of the narrow-line Seyfert 1 galaxy I Zwicky 1: black hole mass. *The Astrophysical Journal* **2019**, *876*, 102. <https://doi.org/10.3847/1538-4357/ab16ef>.
82. Osterbrock, D.E.; Pogge, R.W. The spectra of narrow-line Seyfert 1 galaxies. *The Astrophysical Journal* **1985**, *297*, 166–176. <https://doi.org/10.1086/163513>.

83. Marziani, P.; del Olmo, A.; Negrete, C.A.; Dultzin, D.; Piconcelli, E.; Vietri, G.; Martínez-Aldama, M.L.; D’Onofrio, M.; Bon, E.; Bon, N.; et al. The intermediate-ionization lines as virial broadening estimators for Population A quasars. *The Astrophysical Journal Supplement Series* **2022**, *261*, 30. <https://doi.org/10.3847/1538-4365/ac6fd6>.
84. Kaspi, S.; Smith, P.S.; Netzer, H.; Maoz, D.; Jannuzi, B.T.; Giveon, U. Reverberation Measurements for 17 Quasars and the Size-Mass-Luminosity Relations in Active Galactic Nuclei. *The Astrophysical Journal* **2000**, *533*, 631. <https://doi.org/10.1086/308704>.
85. Panda, S. Physical Conditions in the Low-Ionization Broad-Line Region in Active Galaxies. *Publications de l’Observatoire Astronomique de Beograd* **2021**, *100*, 333–338. <https://doi.org/10.3847/1538-4365/ac6fd6>.
86. Grevesse, N.; Asplund, M.; Sauval, A.; Scott, P. The chemical composition of the sun1This review is part of a Special Issue on the 10th International Colloquium on Atomic Spectra and Oscillator Strengths for Astrophysical and Laboratory Plasmas. *Canadian Journal of Physics* **2011**, *89*, 327–331, [<https://doi.org/10.1139/p10-119>]. <https://doi.org/10.1139/p10-119>.
87. Bottorff, M.C.; Ferland, G.J. Magnetic confinement, magnetohydrodynamic waves and smooth line profiles in active galactic nuclei. *Monthly Notices of the Royal Astronomical Society* **2000**, *316*, 103–106, [<https://academic.oup.com/mnras/article-pdf/316/1/103/3894373/316-1-103.pdf>]. <https://doi.org/10.1046/j.1365-8711.2000.03465.x>.
88. Rees, M.J. Magnetic confinement of broad-line clouds in active galactic nuclei. *Monthly Notices of the Royal Astronomical Society* **1987**, *228*, 47P–50P, [<https://academic.oup.com/mnras/article-pdf/228/1/47P/2807795/mnras228-047P.pdf>]. <https://doi.org/10.1093/mnras/228.1.47P>.
89. Kollatschny, W.; Zetzl, M. The shape of broad-line profiles in active galactic nuclei. *Astronomy & Astrophysics* **2013**, *549*, A100.
90. Marziani, P.; Berton, M.; Panda, S.; Bon, E. Optical Singly-Ionized Iron Emission in Radio-Quiet and Relativistically Jetted Active Galactic Nuclei. *Universe* **2021**, *7*. <https://doi.org/10.3390/universe7120484>.
91. Ferland, G.J.; Persson, S.E. Implications of CA II Emission for Physical Conditions in the Broad-Line Region of Active Galactic Nuclei. *The Astrophysical Journal* **1989**, *347*, 656. <https://doi.org/10.1086/168156>.

**Disclaimer/Publisher’s Note:** The statements, opinions and data contained in all publications are solely those of the individual author(s) and contributor(s) and not of MDPI and/or the editor(s). MDPI and/or the editor(s) disclaim responsibility for any injury to people or property resulting from any ideas, methods, instructions or products referred to in the content.